Journal of Materials Chemistry A

ROYAL SOCIETY OF CHEMISTRY

PAPER

View Article Online
View Journal | View Issue

Cite this: J. Mater. Chem. A, 2022, 10, 2388

Perovskite crystal symmetry and oxygen-ion transport: a molecular-dynamics study of perovskite†

Elisabeth Robens,[a] Robert Rauschen,[a] Johannes Kaub,[a] Jana P. Parras,[a] Dennis Kemp,[a] Colin L. Freeman[b] and Roger A. De Souza *[a]

Received 26th July 2021
Accepted 2nd October 2021

DOI: 10.1039/d1ta06293j

rsc.li/materials-a

Many ABX_3 perovskite compounds adopt at temperatures of interest a low-symmetry structure, rather than the ideal (cubic) structure. The prototypical case is the mineral perovskite ($CaTiO_3$), which exhibits orthorhombic symmetry over a wide range of temperatures, attaining ideal, cubic symmetry only at very high temperatures. In this study, we made use of this behaviour to examine the effect of crystal symmetry on oxygen diffusion in a single perovskite material. Employing molecular dynamics (MD) simulations, we calculated oxygen tracer diffusion coefficients in $CaTiO_3$, doped with various acceptor species, in the range $1000 \leq T/K \leq 2500$. The activation enthalpy of oxygen tracer diffusion was found to be larger for the orthorhombic structure (0.58 eV) than for the cubic structure (0.43 eV). In addition, oxygen tracer diffusion was found to be adversely affected by the presence of acceptor-type cation defects, with stronger effects being observed for the low-symmetry structure. Our results also allow us to suggest explanations for the large scatter observed in experimental transport studies; to derive trends for the alkaline-earth perovskites; and to emphasise the merits of using MD simulations, rather than static calculations, to obtain activation barriers for ion migration in the high-symmetry forms of distorted perovskites.

1 Introduction

Anion transport in ABO_3 perovskite-type oxides is widely believed to occur most readily in those compositions that display the highest symmetry. Indeed, the best perovskite-based oxygen-ion conductors—materials that constitute some of the best oxygen-ion conductors currently known:[1–6] $LaGaO_3$-based electrolytes,[7–9] (Na,Bi)TiO_3-based electrolytes,[10–13] and mixed ionic–electronic conductors in the (La,Ba,Sr)(Co,Fe)O_3 system[14–19]—display cubic symmetry (or small distortions thereof). Quantitative correlations between transport rate and crystal symmetry have suffered, however, from comparisons being made between materials that have different structures and compositions.[20–25] Comparing oxygen-ion conduction, for instance, in cubic $BaZr_{0.9}Y_{0.1}O_{2.95}$ and in orthorhombic $CaZr_{0.9}In_{0.1}O_{2.95}$,[25] one finds faster transport in the higher symmetry system. These two compositions differ, though, not only in terms of their symmetry, but also in terms of their A-site cations (Ba *vs.* Ca) and their acceptor-type substituents (Y *vs.* In). Thus, the effects on ion transport arising from the composition need to be separated from those arising from the crystal symmetry, and this may be far from trivial for concentrated solid solutions. A superior approach would be to study oxygen-ion transport in a single, weakly doped perovskite-type oxide that undergoes with increasing temperature a series of transitions to increasingly higher symmetry forms.

In this sense, the eponymous mineral is an ideal system. $CaTiO_3$ is considered in various studies,[26–29] though not all,[30,31] to undergo the following sequence of symmetry changes with increasing temperature:

$$Pbnm \leftrightarrow Cmcm \leftrightarrow I4/mcm \leftrightarrow Pm\bar{3}m. \quad (1)$$

The transition from orthorhombic *Pbnm* to orthorhombic *Cmcm* occurs at $T = (1380 \pm 10)$ K, with the subsequent transition to tetragonal *I*4/*mcm* occurring at $T = (1500 \pm 20)$ K and the final transition to cubic $Pm\bar{3}m$ at $T = (1600 \pm 10)$ K.[26–29] The intermediate orthorhombic (*Cmcm*) phase is not always observed in experiment,[30,31] and this may be due to its structural and thermodynamic similarity to the orthorhombic *Pbnm* phase.[29] The four phases correspond to tilting of the TiO_6 octahedra about 3, 2, 1 and 0 pseudo-cubic axes, respectively.[32–34]

[a]Institute of Physical Chemistry, RWTH Aachen University, 52056 Aachen, Germany. E-mail: desouza@pc.rwth-aachen.de; Fax: +49 241 80 92128; Tel: +49 241 80 94739
[b]Department of Materials Science and Engineering, University of Sheffield, Sheffield, UK

† Roger De Souza writes: John Kilner played a formative role in my scientific career. He introduced me to the world of defects, diffusion and perovskites some 30 years ago, providing illuminating and captivating guidance. It seems fitting, therefore, to contribute to his Festschrift with a paper on defects and diffusion in the mineral perovskite.

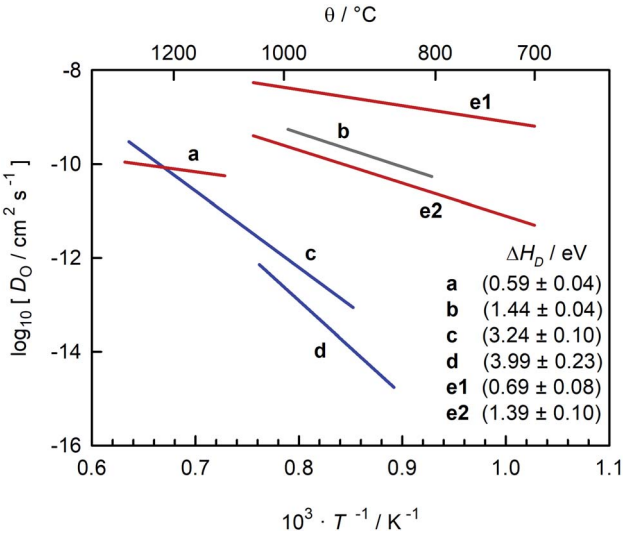

Fig. 1 Comparison of oxygen diffusion coefficients obtained for $CaTiO_3$: a (George and Grace[35]), b (Iwahara *et al.*[36]) c (Gautason and Muehlenbachs[37]), d (Sakaguchi and Haneda[38]), e (Bak *et al.*[39]). Data converted from conductivities (grey), tracer diffusivities (blue), or chemical diffusivities (red). Tracer data converted *via* $D_O = D^*_O/f^*$, with $f^* = 0.69$; chemical data assuming $D_O = D^\delta_O n_v/3$ and $n_v = 1.86 \times 10^{-4}$; and conductivity data *via* the Nernst–Einstein equation.

In a different sense, $CaTiO_3$ is not an ideal system for examining the correlation between symmetry and ion transport. Experimental studies of oxide-ion transport in nominally un-doped $CaTiO_3$ (ref. 35–39) report isothermal oxygen diffusion coefficients that differ by four or more orders of magnitude, with the corresponding activation enthalpies of oxygen diffusion (ΔH_D) scattering between 0.6 eV and 4 eV (see Fig. 1). Some variation in oxygen diffusivity is to be expected, since nominally un-doped samples will contain varying levels of acceptor impurities. But variations in impurity level of four orders of magnitude are implausible in this case, and such variations cannot explain the large scatter in reported activation enthalpies.

A closer examination indicates that the activation enthalpies fall puzzlingly into three groups, with $\Delta H_D \approx 0.6$ eV,[35,39] $\Delta H_D \approx 1.4$ eV,[36,39] and $\Delta H_D > 3$ eV.[37,38] Equally puzzling is the huge discrepancy between studies that are often regarded as unambiguous: the activation barrier for oxygen-vacancy migration in orthorhombic $CaTiO_3$ was reported in classical[40,41] and quantum-mechanical[42] simulations to be <1 eV, whereas tracer diffusion measurements of single crystals yield $\Delta H_D \approx 4$ eV.[38] Furthermore, the problems, whatever they are, do not afflict all $CaTiO_3$-based systems. All studies of oxygen diffusion in $CaTi_{0.9}Fe_{0.1}O_{3-\delta}$ agree, as pointed out by Salles *et al.*,[43] that the activation enthalpy of diffusion is $\Delta H_D \approx 0.9$ eV.[43–46]

In this study, we performed classical molecular dynamics (MD) simulations of oxygen tracer diffusion in $CaTiO_3$ as a function of temperature, first, in order to bring some clarity to published experimental data;[35–39] and second, in order to examine the relationship between crystal symmetry and oxygen-ion transport in a perovskite-type oxide. There are two benefits to carrying out MD simulations of ion transport. Data interpretation does not have to rely solely on the activation enthalpy (as is the case for static simulations) but can also make use of the absolute magnitude of the oxygen diffusivity. And in comparison with experimental work, the number and type of point defects are known exactly for the systems under study.

Lastly, we comment on our choice of classical MD simulations over MD simulations based on Density-Functional-Theory (DFT) calculations. The latter are restricted currently to short simulation times, very small simulation cells, and often, excessively high simulation temperatures. These restrictions translate into inadequate statistics (*i.e.* an insufficiently large number of successful ion jumps, and thus imprecise diffusion data); extremely high defect concentrations (*i.e.* well beyond the limit of a dilute solution); and the necessity to extrapolate data from temperatures several thousand kelvin above the solid's melting point down to the temperatures of experimental interest. Our choice of classical MD simulations was dictated, therefore, by the need to obtain precise diffusion data for dilute solutions of point defects at physically reasonable temperatures.

Classical MD simulations, it is sometimes claimed, are unsuited for studying ion migration in solids, for they do not include bond breaking and formation. Such claims appear to be based mainly on misconceptions of both the simulation methods and the migration process. They also ignore entirely a substantial body of evidence. For example, classical simulation methods employing the set of empirical pair potentials (EPP) derived by Pedone *et al.*[47] are able to predict quantitatively the rate of defect migration and its temperature dependence for oxygen-vacancy diffusion in $BaTiO_3$,[48–51] and for oxygen-vacancy diffusion[52–57] and strontium-vacancy diffusion[58–60] in $SrTiO_3$. If ion migration did involve bond breaking and bond formation, such agreement between simulation and experiment would be impossible: there would always be discrepancies, and this is not the case. Given the evident capabilities of the EPP set derived by Pedone *et al.*[47] for quantitatively describing ion migration in $BaTiO_3$ and $SrTiO_3$, we employ them here to study oxygen diffusion in $CaTiO_3$.

2 Computational

In all simulations performed in this study, the constituent ions of the solid were treated as classical particles, each bearing a charge and interacting with other particles through a long-range coulombic potential and a short-range EPP. As noted

Table 1 Empirical pair-potential (EPP) parameters used in this study. Values were taken from Pedone *et al.*[47] without modification

Ion pair	D_{ij}/meV	a_{ij}/Å^{-1}	r_0/Å	C_{ij}/eV Å^{12}
$Ca^{+1.2}$–$O^{-1.2}$	30.211	2.241334	2.923245	5.0
$Ti^{+2.4}$–$O^{-1.2}$	24.235	2.254703	2.708943	1.0
$Al^{+1.8}$–$O^{-1.2}$	361.581	1.900442	2.164818	0.9
$Fe^{+1.8}$–$O^{-1.2}$	418.981	1.620376	2.382183	2.0
$O^{-1.2}$–$O^{-1.2}$	42.395	1.379316	3.618701	22.0

above, we used the pairwise potentials derived by Pedone *et al.*,[47] in which ions bear partial charges and the short-range interactions are described by a Morse function and an additional repulsive (r^{-12}) term. That is, the potential between ions i and j as a function of separation r takes the form of

$$\phi_{ij}(r) = \frac{z_i z_j e^2}{r} + D_{ij}\left[\left\{1 - e^{-a_{ij}(r-r_0)}\right\}^2 - 1\right] + \frac{C_{ij}}{r^{12}}. \quad (2)$$

The values for the empirical parameters (D_{ij}, a_{ij}, r_0 and C_{ij}) were taken directly from Pedone *et al.*[47] and are summarized in Table 1. Long-range coulombic interactions were evaluated by an Ewald summation[61] with an accuracy of 10^{-6}, and short-range interactions were evaluated up to 15 Å.

The MD simulation cell consisted of 12 × 12 × 12 unit cells of $Ca_4Ti_4O_{12}$ (34 560 ions) with periodic boundary conditions applied in all three spatial directions. Point defects were introduced by either removing or replacing ions at random from the simulation cell. If the total charge of all defects was not zero, the excess was compensated by means of an uniform background charge. MD simulations were performed within the *NpT* ensemble, *i.e.*, particle number N, pressure p and temperature T were held constant, while energy U and volume V were allowed to vary. The system's temperature (pressure) was controlled by means of a Nose–Hoover thermostat (barostat), with damping parameters of 1 ps (10 ps). A timestep of 1 fs was used. The LAMMPS (Large-scale Atomic/Molecular Massively Parallel Simulator) code[62] was used.

For each MD simulation, the cell was first allowed to equilibrate for 40 ps (after which U and V were observed to only fluctuate around constant values). Thereafter, the simulation was run for 500 ps, and the mean-squared-displacement of the oxide ions $\langle R_O^2 \rangle$ was monitored. For every simulation in which the evolution of $\langle R_O^2 \rangle$ as a function of time was smooth and linear, we calculated a tracer diffusion coefficient of oxygen from the standard Einstein relation

$$D_O^* = \frac{1}{6}\frac{d\langle R_O^2 \rangle}{dt}. \quad (3)$$

The activation barriers for oxygen-ion migration were also determined by means of molecular-statics simulations. Climbing-image nudged-elastic-band (CI-NEB) calculations were performed at constant volume with 25 images, as implemented in the GULP code.[63] The (static) lattice energies of various $CaTiO_3$ perovskite phases were also calculated with the GULP code.

3 Results

In correlating crystal symmetry and ion transport, one needs to identify the exact phase in which ion transport is taking place. In the present case, that meant we had to identify the phases that this set of EPP yield in the MD simulations before we studied oxygen diffusion. In fact, we took a step back and considered first the relative (static) lattice energies of various $CaTiO_3$ perovskite phases.

3.1 Lattice energies

Although it is now universally agreed that the $CaTiO_3$ lattice displays *Pbnm* symmetry at room temperature and adopts $Pm\bar{3}m$ symmetry at sufficiently high temperature, there are debates concerning the intermediate phases. It has been argued that a direct transition is unlikely,[32–34] so that the question is not so much whether there are intermediate phases but rather what the intermediate phases are.

Taking our lead from Amisi *et al.*,[64] who studied the crystal structures of the related perovskite $SrZrO_3$ and their instabilities with regard to octahedral tilting, we performed energy minimisation calculations of the most likely perovskite crystal symmetries of $CaTiO_3$ [see sequence eqn (1)], as well as of some possible alternatives. The results are shown in Fig. 2. Examining the differences in lattice energy relative to that of the cubic phase, we find that, according to these EPP, intermediate orthorhombic and tetragonal phases are plausible, with *Cmcm* being preferred over *Imma* for the intermediate orthorhombic phase and *I*4/*mcm* being preferred over *P*4/*mbm* for the intermediate tetragonal phase. Our static simulations are thus in agreement with data from calorimetry,[26] Raman spectroscopy,[27] neutron powder diffraction,[28] and thermodynamic modelling[29] studies.

3.2 Temperature-dependent lattice parameters

In Fig. 3(a) we plot the pseudo-cubic lattice parameters obtained for $CaTiO_3$ in our MD simulations. Changes in the behaviour are observed at $T_{1/2} = (1225 \pm 5)$ K, $T_{2/3} = (1295 \pm 5)$ K, and $T_{3/4} = (1335 \pm 5)$ K. From these data it is not possible to identify the exact space group, but it is evident that phase 1 is orthorhombic ($a_{pc} \neq b_{pc} \neq c_{pc}$); phase 3 is tetragonal ($a_{pc} = b_{pc} < c_{pc}$); and phase 4 is cubic ($a_{pc} = b_{pc} = c_{pc}$). Phase 2 appears to be tetragonal, but a_{pc} and b_{pc} are only approximately equal and

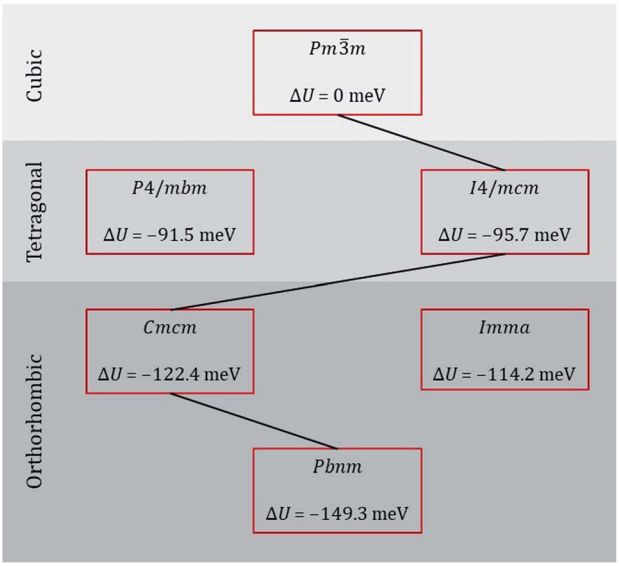

Fig. 2 Lattice energy U of various phases of $CaTiO_3$ relative to that of the ideal cubic phase. The black line indicates the probable sequence of transitions.

close examination indicates $a_{pc} \neq b_{pc} \neq c_{pc}$. On the basis of the results obtained in the previous section, we ascribe phases 1–4 to *Pbnm*, *Cmcm*, *I*4/*mcm* and *Pm*$\bar{3}$*m* space groups.

These transition temperatures are much lower than the experimental values[26,28,29] of $T = (1380 \pm 10)$ K, $T = (1500 \pm 20)$ K and $T = (1600 \pm 10)$ K. The differences between simulation and experiment get larger, the higher the transition temperature. This is not particularly surprising, though, since these EPP were not fitted to crystal data for $CaTiO_3$ (but to data for binary oxides and glasses[47]). Here, it is sufficient that different phases are stable in the MD simulations because it means that MD simulations with these EPP can be used to examine oxygen diffusion in these different phases.

Upon introducing oxygen vacancies into the simulation cell at a site fraction of $n_v = 0.2\%$ (and compensating their charge with a background charge), we observed that the transition temperatures shifted to lower values [Fig. 3(b)]: (1180 ± 20) K, (1210 ± 10) K, and (1250 ± 10) K. We believe that the direction of the shifts is predicted correctly because increasing x in the $CaTi_{1-x}Fe_xO_{3-x/2}$ system decreases the transition temperatures[65] and because reducing $BaTiO_3$ decreases the ferroelectric–paraelectric transition temperature.[51] The magnitude of the shifts (up to 85 K) are rather large, though, and we cannot rule out that these shifts are overestimated. Nevertheless, the data of Fig. 3 do clearly indicate that there is an effect from oxygen vacancies alone, their charge being compensated in these specific simulations by a background charge. In experiment, a compensating defect is always present, *e.g.* acceptor substituents or electrons produced upon sample reduction, and this complicates the assignment to a specific point defect.

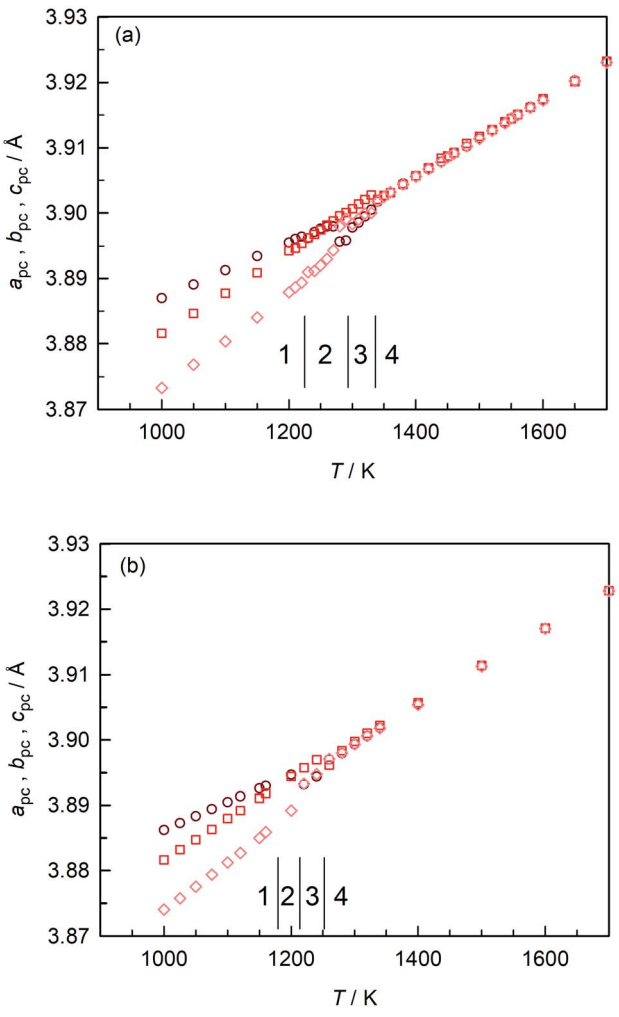

Fig. 3 Pseudo-cubic lattice parameters obtained as a function of temperature: (a) stoichiometric $CaTiO_3$; (b) oxygen-deficient $CaTiO_3$.

3.3 Oxygen tracer diffusion

We first consider oxygen tracer diffusion in a system containing only oxygen vacancies, since this allows us to examine the dynamic behaviour of oxygen vacancies without having to take interactions with acceptor cations into account. Subsequently, we consider oxygen diffusion in systems with the same number of vacancies but also containing specific acceptor cations as charge compensation. All data presented in this section refer to cells containing 0.2% oxygen vacancies (or 42 vacancies in a cell containing 20 736 oxygen-ion sites).

Oxygen tracer diffusion coefficients obtained for the system with only oxygen vacancies as a function of temperature are shown in Fig. 4(a). The temperatures of the phase transitions determined in Sec. 3.2 are also shown, and there are no evident jumps in D_O^* at these temperatures. For the two intermediate phases, the stability ranges are too small to allow activation enthalpies to be determined. We focus, therefore, on the end phases and obtain activation enthalpies of $\Delta H_{D^*} = (0.584 \pm 0.017)$ eV for the *Pbnm* phase and of $\Delta H_{D^*} = (0.429 \pm 0.004)$ eV for the *Pm*$\bar{3}$*m* phase. The tracer diffusion of oxygen is clearly characterised by a far larger activation enthalpy in the low-symmetry phase.

In Fig. 4(b), the ratios of the axis-specific tracer diffusion coefficients are plotted, $D_O^{*,y}/D_O^{*,x}$, and $D_O^{*,z}/D_O^{*,x}$. This plot confirms the analysis of Sec. 3.2, since the two ratios are both approximately unity for the isotropic *Pm*$\bar{3}$*m* phase but differ substantially from unity and from one another for the non-isotropic *Pbnm* phase. Incidentally, the two intermediate phases behave as expected: in the tetragonal phase, one ratio is approximately unity and one isn't; and for the intermediate orthorhombic phase, both ratios deviate from unity.

In Fig. 5(a) and (b) we examine the effect of compensating acceptor-type defects on D_O^* (at constant $n_v = 0.2\%$). The data are divided into native (divalent) acceptor-type species (v_{Ca}, Ca_{Ti}) and foreign (trivalent) acceptor-type species (Al_{Ti}, Fe_{Ti}). No reliable data was obtained for cells containing v_{Ti} and v_O, or at lower temperatures for cells containing Ca_{Ti} and v_O, or Al_{Ti} and v_O. As expected,[13,66–68] all acceptor-species cause the rate of oxygen diffusion at a given temperature to decrease (even though the vacancy site fraction is constant) and the effective activation enthalpy to increase. The effects are stronger for the lower-symmetry phase, as indicated by the larger increases in ΔH_{D^*}. For example, in the presence of v_{Ca}, the activation enthalpy of oxygen diffusion increases by 0.13 eV for the cubic phase but by 0.33 eV for the orthorhombic phase. The changes in D_O^* and ΔH_{D^*} can be attributed to acceptor-type cation defects

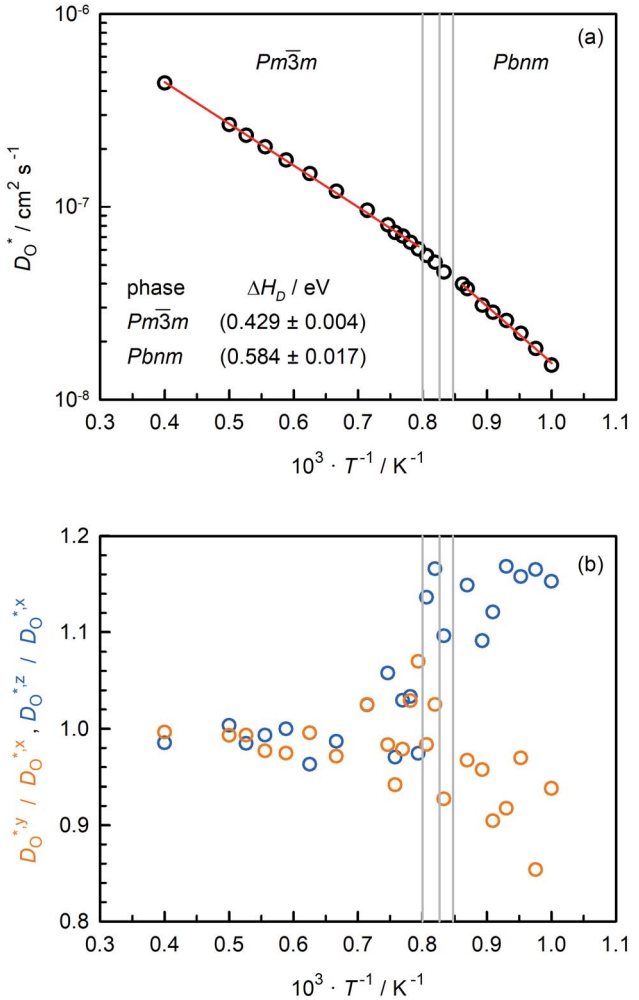

Fig. 4 Oxygen tracer diffusion coefficients obtained for a $CaTiO_3$ system containing only oxygen vacancies as a function of inverse temperature: (a) total values, (b) ratios of axis-specific values. Error bars are smaller than the symbol size.

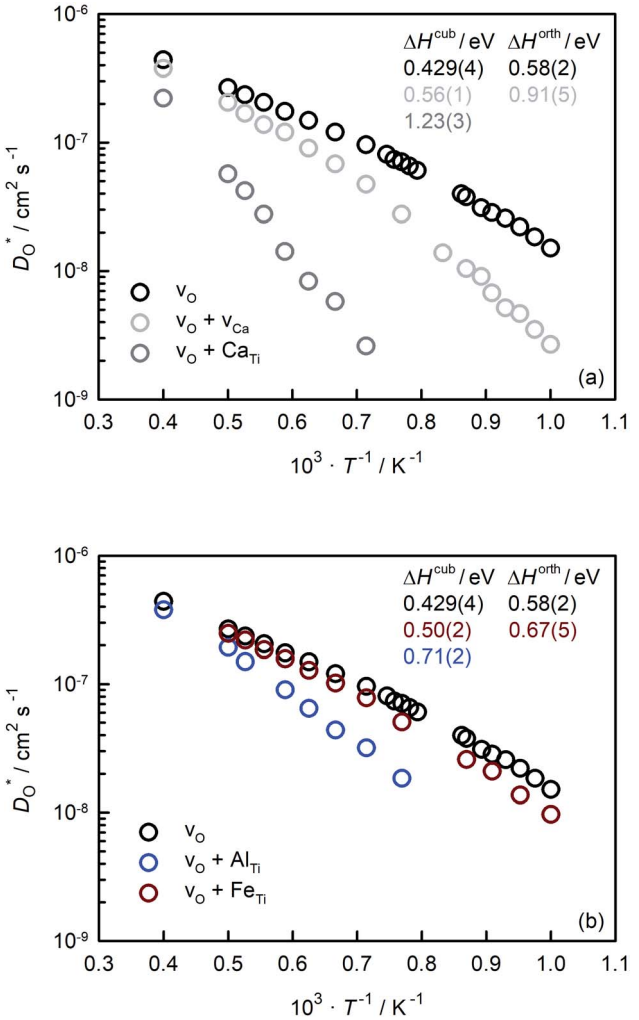

Fig. 5 Tracer diffusion coefficients of oxygen obtained for $CaTiO_3$ with oxygen vacancies and charge-compensating acceptor-type defects: (a) native acceptor defects, (b) foreign acceptor defects. In all cases, the site fraction of oxygen vacancies was $n_v = 0.2\%$.

trapping oxygen vacancies in their vicinity and modifying the barriers for oxygen-vacancy migration in their vicinity.[66] The use of a background charge works as a 'perfect' acceptor-dopant, introducing v_O, but not affecting their behaviour.

3.4 Activation barriers from static calculations

There are eight oxygen ions that can jump into a neighbouring vacant site in the perovskite structure. In the un-doped cubic phase, all eight jumps are symmetry equivalent, and hence, oxygen-vacancy migration is characterised by one single barrier. In the un-doped *Pbnm* phase, there are five symmetry-inequivalent jumps. Introducing acceptor-type cation species into these lattices modifies the barriers for ion migration not only around but also towards and away from the acceptor-type species,[66] generating a more complex energy landscape with multiple possible barriers even for the cubic phase. For this reason, and also to make two specific points, we focus here on migration in the un-doped phases (*i.e.* in those containing only oxygen vacancies).

The activation barriers determined for the five jumps in the un-doped, orthorhombic phase by means of NEB calculations are listed in Table 2. The effective activation enthalpy of long-range oxygen diffusion will be a weighted means of those barriers that connected together provide low-energy paths through the structure. Consideration of how the barriers listed in Table 2 are connected indicates that the highest barrier of 0.73 eV does not need to be traversed for long-range diffusion. This leaves barriers that are rather similar, of 0.54 eV, 0.60 eV, 0.61 eV and 0.63 eV. Given these possibilities, ions will jump most often over the lowest barrier, but also over the other barriers, since the relative jump rates at the temperatures of interest [$\propto \exp(-\Delta H_{mig,v}/k_B T)$] do not differ by orders of magnitude. This picture is consistent with the effective activation enthalpy of oxygen diffusion of (0.584 ± 0.017) eV obtained in the MD simulations.

NEB calculations of oxygen-ion migration in the $Pm\bar{3}m$ phase were unreliable: with a $4 \times 4 \times 4$ supercell of cubic $CaTiO_3$, an

activation barrier of 0.59 eV was obtained, and with a $6 \times 6 \times 6$ supercell, 0.57 eV. These values, though physically reasonable, are clearly representative of the orthorhombic structure, rather than of the (starting) cubic structure [*cf.* Fig. 4(a)]. The problem is that NEB calculations refer to zero kelvin, and at this temperature the *Pbnm* phase, with its tilted octahedra, has the lowest energy. Examination of the NEB simulation cells indicated that coordinated tilting of the octahedra had indeed occurred. Although even-number-sized supercells are obligatory for coordinated tilting of the octahedra to occur, the use of an odd-number-sized supercell, *e.g.* $3 \times 3 \times 3$, produced unreasonable results, namely, an asymmetric energy profile with an intermediate minimum, whose maximal barrier height was only 0.17 eV. NB: all problems encountered in NEB calculations of oxygen-vacancy migration in cubic $CaTiO_3$ did not plague analogous calculations for $SrTiO_3$, whose ground state structure, according to these EPP, is cubic.

In order to frustrate the coordinated tilting of the octahedra, one could perform Mott–Littleton (ML) calculations[69] with a relatively small inner region I. As ionic relaxations are only fully permitted within region I and not within the adjacent region IIa, the alignment of tilts between regions I and IIa can in principle force the system to maintain artificially high symmetry. We found that a region I size of *ca.* 7 Å yielded an activation barrier of oxygen-vacancy migration in the cubic structure of 0.42 eV, a value consistent with the MD results. Evidently, this region I size is sufficient to capture ionic relaxation for both the initial and transition-state configurations and prevent octahedral tilting from occurring.

In general, it may be difficult to determine definitively from a molecular-statics simulation (NEB or ML) whether a specific initial or transition-state configuration exhibits distortions characteristic of a lower symmetry phase. It is only because we have values from MD simulations at finite temperatures that we are able to judge the fidelity of the barriers obtained from NEB and ML calculations.

4 Discussion

4.1 Comparison with experimental data for $CaTiO_3$

The best level for comparing transport data is at the level of defect diffusivities because D_v is independent of defect concentration, at least for non-interacting solutions of charge carriers. D_v can be obtained from D_O^* according to

$$D_v = \frac{D_O^*}{f^* n_v}, \tag{4}$$

where f^* is the tracer correlation coefficient. For oxygen-vacancy migration in a cubic perovskite, $f^* = 0.69$.[70] Here for simplicity we also apply this value to data obtained for the non-cubic phase, aware that f^* may take a different value for diffusion in a distorted perovskite.

Another benefit of considering D_v is that its temperature dependence directly yields the activation enthalpy of oxygen-vacancy migration,

$$\Delta H_{mig,v} = -k_B \frac{d \ln D_v}{d(1/T)}. \tag{5}$$

In contrast, the activation enthalpy of oxygen diffusion is the sum of $\Delta H_{mig,v}$ and $\Delta H_{gen,v}$, the latter indicating how strongly n_v varies with temperature:

$$\Delta H_{gen,v} = -k_B \frac{d \ln n_v}{d(1/T)}. \tag{6}$$

In Fig. 6 we compare oxygen-vacancy diffusivities with the two sets of literature data for which the vacancy diffusivity can be confidently calculated from oxygen diffusion data.[35,39] (The reason for confidence is that, if chemical diffusion is examined in a regime for which the electronic conductivity dominates the overall conductivity, D_v is simply given by $D_O^{\delta}/3$.)[25] One finds that the closest agreement in terms of absolute magnitude is with dataset e1.[39] The difference between experiment and simulation could be due to one or more factors: f^* for oxygen-vacancy migration in an orthorhombic perovskite differing from the value for the cubic structure; a slight overestimation of D_v in the MD simulations; or a slightly underestimation of D_v in the chemical diffusion experiments. At present none of these possibilities can be ruled out. The experimental activation enthalpy appears to be too high, $\Delta H_{mig,v} = (0.69 \pm 0.08)$ eV,[39] but the error is substantial. [And $\Delta H_{mig,v}$ decreases to (0.59 ± 0.17) eV if, for example, the lowest-temperature data point is ignored.] Importantly, one recognises from Fig. 6 that agreement in terms of activation enthalpy is not sufficient to judge data. There is a substantial difference in vacancy diffusivities between datasets a and f, even though the activation enthalpies agree well.

The oxygen diffusion coefficients obtained in tracer diffusion studies[37,38] are, as shown in Fig. 1, orders of magnitude lower than the dataset e1 of Bak *et al.*,[39] and they have very high activation enthalpies. We suggest that these tracer diffusion data are incorrect for two reasons. First, in both cases the interpretation of the experimental data is questionable. Sakaguchi and Haneda[38] obtained isotope profiles in the solid—isotope profiles with two features, and they attributed the first feature to bulk diffusion and the second to fast-diffusion along twin boundaries. We propose that the correct assignment of the two features is to diffusion through a depletion space-charge layer followed by diffusion in a homogeneous bulk phase.[71,72] A surface space-charge zone has already been identified previously for acceptor-doped $SrTiO_3$,[55,73–76] acceptor-doped $BaTiO_3$,[49]

Table 2 Activation enthalpies for the five symmetry-inequivalent jumps of oxygen ions into neighbouring vacancies in orthorhombic $CaTiO_3$ obtained by NEB calculations. O1 is the apical site and O2 the equatorial site of the TiO_6 octahedron. The two sites differ in energy by only 0.1 eV; this means that there is a small difference in enthalpies for forward and backward jumps, but this difference can be ignored

Jump	$\Delta H_{mig,v}$/eV
O1–O2	0.61
O1–O2	0.54
O1–O2	0.73
O2–O2	0.60
O2–O2	0.63

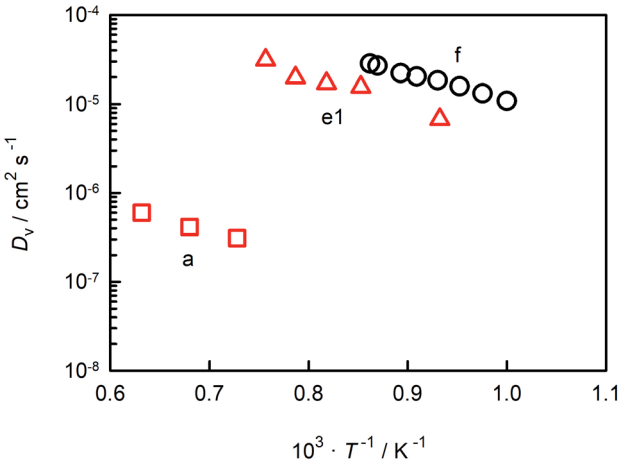

Fig. 6 Oxygen-vacancy diffusion coefficients in $CaTiO_3$ as a function of inverse temperature: a (George and Grace[35]), e1 (Bak *et al.*[39]), f (this study).

and for acceptor-doped Pb(Zr,Ti)O_3.[77,78] It would be extremely surprising if acceptor-doped $CaTiO_3$ did not have a depletion space-charge zone at its surface. One consequence of an incorrect assignment would be that the conclusion of Sakaguchi and Haneda,[38] of fast oxygen diffusion along domain walls, would be incorrect, too. In the other tracer study, Gautason and Muehlenbachs[37] conducted gas-phase monitoring of isotope exchange and assumed that the kinetics were governed by bulk diffusion. They employed, however, powdered samples, and for such samples, the exchange kinetics are generally limited by the process of surface exchange.[79,80] In fact, their activation enthalpy of (3.24 ± 0.10) eV[37] is reasonably close to the activation enthalpy of isotope exchange measured for acceptor-doped $SrTiO_3$, $\Delta H_{k*} \approx 3$ eV.[55] In other words, in both cases[37,38] there are more plausible explanations for the low values of D_O^* and for the high values of ΔH_{D*}.

The second reason to question the tracer diffusion data[37,38] is that the high values of ΔH_{D*} require $\Delta H_{mig,v}$ to be improbably high. Under the oxidising conditions of the experiments, typical fixed-valence acceptor impurities in perovskite titanates, such as Mg and Al, yield $\Delta H_{gen,v} \approx 0$, while variable valence acceptor dopants, such as Fe, yield $\Delta H_{gen,v} = (0.1$ to $0.2)$ eV.[81] As a consequence, $\Delta H_{mig,v}$ $(=\Delta H_{D*} - \Delta H_{gen,v})$ would have to be (3 to 4) eV, which seems very unlikely.

Lastly, even though there are no experimental results for the cubic phase with which to compare our MD data, we contend that the data are fairly accurate, in particular the small activation enthalpy of oxygen-vacancy migration of 0.43 eV, because our data for the orthorhombic structure are in good agreement with experiment and because MD data for $SrTiO_3$ and $BaTiO_3$ obtained with these EPP show excellent agreement with literature values.[49,51–55,57]

4.2 Comparison with computational data for $CaTiO_3$

There are three static computational studies of oxygen-ion migration by a vacancy mechanism in $CaTiO_3$. Two studies[40,41] employed Mott–Littleton calculations, with different sets of EPP to the set used here, and reported for *Pbnm* symmetry a single barrier[40] of 0.58 eV and three barriers[41] of 0.51 eV, 0.43 eV and 0.55 eV for migration along the three axes of the orthorhombic unit cell. These data are in reasonable agreement with our NEB results [five barriers between 0.54 eV and 0.73 eV, see Table 2] and with our MD results [an effective activation enthalpy of (0.584 ± 0.017) eV, see Fig. 4(a)].

A more recent DFT study[42] reported, for small supercells with either *Pbnm* or *Pm*$\bar{3}$*m* starting symmetry, activation barriers that are suspiciously similar, at 0.71 eV and 0.75 eV, and that are too high. On the basis of our NEB and ML simulations (Sec. 3.4), we suggest that the similarity is an artefact, arising from octahedral tilting in the cubic supercell. And on the basis of the systematic DFT study of oxygen-vacancy migration in $SrTiO_3$ by Zhang *et al.*,[57] we suggest that the use of small supercells is responsible for the overestimation of the activation barriers.

4.3 $CaTiO_3$ *versus* other titanate perovskites

Fig. 7(a) compares the oxygen-vacancy diffusivity calculated in this study for $CaTiO_3$ with those reported in the literature for $SrTiO_3$ (ref. 56) and $BaTiO_3$.[50] The three datasets are strictly comparable, as they all were obtained from MD simulations with the EPP of Pedone *et al.*[47] and refer to dilute solutions of non-interacting oxygen vacancies. (As noted in the Introduction, the MD data for $SrTiO_3$ and $BaTiO_3$ show excellent agreement with experimental values.[49,51–55]) Isothermal values of D_v are seen to increase in the order: $D_v(BaTiO_3) < D_v(SrTiO_3) < D_v(CaTiO_3)$. The temperature dependence, *i.e.* $\Delta H_{mig,v}$, decreases in the same order. Particularly surprising is that orthorhombic $CaTiO_3$ displays faster rates of oxygen-vacancy diffusion with a lower activation enthalpy of migration than cubic $SrTiO_3$. Evidently, symmetry is not the decisive factor in determining the activation barrier, but it is an important factor, as indicated by $\Delta H_{mig,v}^{cub} < \Delta H_{mig,v}^{orth}$ for $CaTiO_3$.

Also of interest is how the behaviour evident in Fig. 7(a) changes upon the addition of acceptor species. Regardless of whether weakly doped material or a solid solution containing high concentrations of oxygen vacancies and acceptor cations, the general trend of Fig. 7(a), we suppose, will be maintained. (And Fe substitution will shift the phase transition temperatures for $CaTiO_3$.[65]) Acceptor species will for each of the three systems decrease the rate of oxygen diffusion and increase its activation enthalpy, maybe not all to exactly the same degree but certainly not to hugely varying degrees. With the exception of Fe-doped $SrTiO_3$,[82] there are no experimental transport data for weakly doped systems. But for 10–20% Fe-substituted systems, the limited experimental evidence[43,83,84] appears to support this supposition: oxygen diffusion is fastest in the $CaTiO_3$-based system and slowest in the analogous $BaTiO_3$-based system.

One reason for comparing the behaviour of these perovskites is to identify trends, and in this way, superior ion-conducting perovskites. Over the years, researchers have attempted to link isothermal conductivities or activation enthalpies to characteristic structural parameters, such as lattice volume, lattice free volume, the critical radius at the transition state, or the Goldschmidt tolerance factor.[22–24,84–86] Here, we examine $\Delta H_{mig,v}$ for these three perovskites as a function of the Goldschmidt

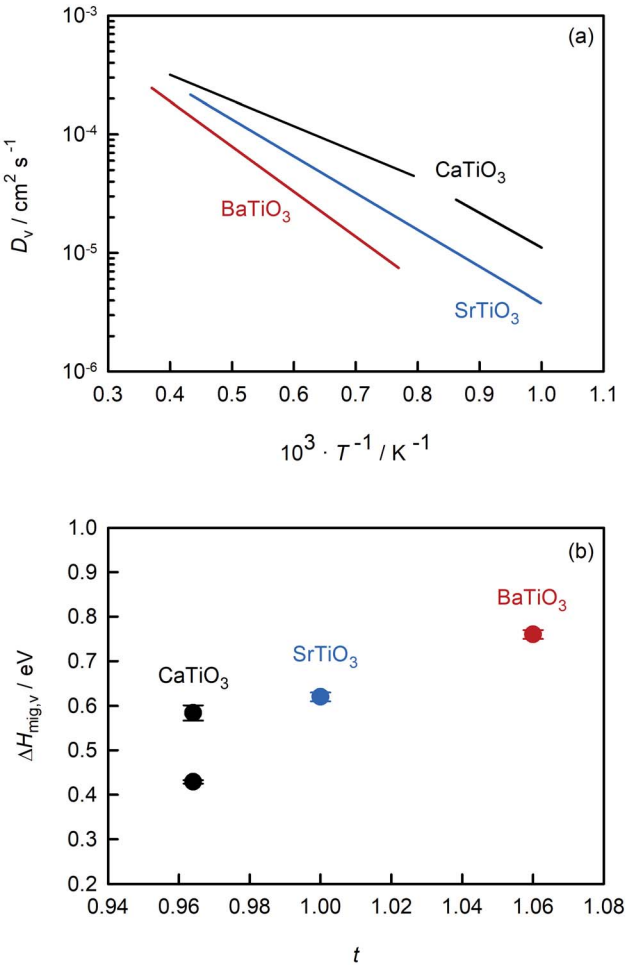

Fig. 7 Comparison of data for titanate perovskites obtained from MD simulations: (a) oxygen-vacancy diffusivities *versus* inverse temperature, (b) activation enthalpy for oxygen-vacancy migration *versus* Goldschmidt tolerance factor. $CaTiO_3$ (this study), $SrTiO_3$ (Waldow and De Souza[56]), $BaTiO_3$ (Kaub *et al.*[50]).

tolerance factor t. We have restricted the analysis to these alkaline-earth titanates because the data refer to the diffusion of non-interacting vacancies and are thus strictly and directly comparable with each other; and we restrict the analysis to this one parameter (t), not because it is the best descriptor (we don't believe it is), but because it is useful for our discussions, *i.e.*, it allows us to make several specific points.

The Goldschmidt tolerance factor is defined as[87]

$$t = \frac{r_A + r_X}{\sqrt{2}(r_B + r_X)}, \quad (7)$$

where r_A, r_B and r_X are the radii of the A, B and X ions in the ABX_3 perovskite structure; numerical values for the radii were taken from Shannon,[88] and since these radii refer to room temperature, so do the calculated tolerance factors. In Fig. 7(b) the activation enthalpy of vacancy migration for these three perovskites is seen to decrease with decreasing tolerance factor. Although the trend suggests that even smaller t would lead to even lower $\Delta H_{mig,v}$, we are wary of extrapolating to smaller t, primarily because of the study of Hayashi *et al.*[22] In their detailed analysis of experimental data, Hayashi *et al.*[22] ascertained that the highest oxygen-ion conductivities of acceptor-substituted $A^{3+}B^{3+}O_3$ perovskites were observed for $t = 0.96$. If this result also holds for $A^{2+}B^{4+}O_3$ perovskites, $CaTiO_3$ is close to the optimum. In other words, for $A^{2+}B^{4+}O_3$ perovskites with $t < 0.96$, $\Delta H_{mig,v}$ would increase from this minimum. There are oxygen transport data that are consistent with this hypothesis, but they do refer to heavily substituted compositions. The effective activation enthalpy of vacancy migration in $SrZr_{0.9}Y_{0.1}O_{2.95}$,[89] for example, is $\Delta H_{mig,v} \approx 1$ eV ($SrZrO_3$, $t = 0.95$), and it is even higher in $CaZr_{0.9}In_{0.1}O_{2.95}$,[90,91] being (2.3 to 2.5) eV ($CaZrO_3$, $t = 0.91$). Also consistent with this hypothesis is the small value of $\Delta H^{cub}_{mig,v} \approx 0.4$ eV we obtained for $CaTiO_3$. Since it is so small and since (to the best of our knowledge) substantially smaller values have not been reported for long-range oxygen diffusion in a perovskite-type oxide [activation enthalpies of *ca.* 0.4 eV have been reported for (Na,Bi)TiO_3 materials[12]], the implication is that $CaTiO_3$ is close to the minimum.

An optimal tolerance factor of $t = 0.96$ suggests that small degrees of structural distortion away from the ideal cubic form are beneficial for oxygen-ion transport, but high degrees are detrimental. This would account for orthorhombic $CaTiO_3$ exhibiting higher oxygen diffusivity than cubic $SrTiO_3$ [Fig. 7(a)], but it would not explain why. This brings us to the major, open question: what is so special about a tolerance factor of $t = 0.96$? Hayashi *et al.*[22] proposed that $t = 0.96$ represents a balance between the tolerance factor and the specific free volume (the proportion of a unit cell not occupied by the ions). Regardless of whether this is correct or not, the larger issue is that, as pointed out by Mogensen *et al.*,[23] this proposal does not explain why optimal behaviour occurs at $t = 0.96$. And at present it is still not clear. A detailed study based on the working hypothesis that Coulomb interactions play the key role in determining the migration barrier for X moieties in ABX_3 perovskites[13,92,93] is underway.

5 Concluding remarks

We performed molecular-dynamics simulations of oxygen-deficient $CaTiO_3$, obtaining oxygen tracer diffusion coefficients for *Pbnm* (orthorhombic) and $Pm\bar{3}m$ (cubic) phases. From these data we determined activation enthalpies of oxygen tracer diffusion (for non-interacting oxygen vacancies) of $\Delta H^{orth}_{mig,v} = (0.584 \pm 0.017)$ eV and $\Delta H^{cub}_{mig,v} = (0.429 \pm 0.004)$ eV. We thus show that for a single, weakly doped perovskite system the lower symmetry phase exhibits a larger activation enthalpy of oxygen diffusion.

The second major result concerns the effect of acceptor-type cation defects (vacancies, antisites, dopants) on oxygen diffusion. We found that their presence decreases the oxygen tracer diffusivity and increases its activation enthalpy, as for other perovskites, and we discovered that these decreases in D^*_O and increases in ΔH_{D^*} are more pronounced for the low-symmetry phase.

Third, based on an analysis of diffusion data for the alkaline-earth titanate perovskites, we showed that orthorhombic $CaTiO_3$ displays faster rates of oxygen-vacancy diffusion with

a lower activation enthalpy of migration than cubic $SrTiO_3$, and we argued in favour of the hypothesis that the rate of oxygen diffusion in perovskite oxides reaches a maximum for those systems with a Goldschmidt tolerance factor of $t = 0.96$. The origin of this behaviour remains unclear.

Fourth, we demonstrated two particular benefits of classical MD simulations. For the orthorhombic phase, with its multiple activation barriers, MD simulations yielded data that refer to long-range diffusion and are thus directly comparable with experimental values. For the cubic phase, which is only stable at elevated temperatures, the MD simulations provided a reliable method for obtaining the activation barrier of ion migration. NEB calculations of ion migration in the cubic phase were found to be unreliable. This is an intrinsic problem afflicting static supercell calculations of ion migration in the high-symmetry phases of ABX_3 perovskites whose ground state structure has lower symmetry.

Lastly, this study constitutes another example of classical MD simulations providing as a function of temperature precise diffusion coefficients that allow experimental transport data for perovskite materials to be clarified and interpreted.[50,68,94] Standard *ab initio* MD cannot be relied upon, but *ab initio* metadynamics simulations[95] do offer exciting possibilities.

Conflicts of interest

There are no conflicts to declare.

Acknowledgements

Funding from German Research Foundation (DFG) within the framework of the collaborative research centre SFB917, "Nanoswitches", is gratefully acknowledged. Simulations were performed with computing resources granted by RWTH Aachen University under projects thes0229, thes0847, rwth0254 and rwth0655.

Notes and references

1 B. C. H. Steele, *Mater. Sci. Eng., B*, 1992, **13**, 79–87.
2 J. C. Boivin and G. Mairesse, *Chem. Mater.*, 1998, **10**, 2870–2888.
3 V. Kharton, F. Marques and A. Atkinson, *Solid State Ionics*, 2004, **174**, 135–149.
4 S. Hull, *Rep. Prog. Phys.*, 2004, **67**, 1233–1314.
5 A. Orera and P. R. Slater, *Chem. Mater.*, 2010, **22**, 675–690.
6 J. A. Kilner and M. Burriel, *Annu. Rev. Mater. Res.*, 2014, **44**, 365–393.
7 T. Ishihara, H. Matsuda and Y. Takita, *J. Am. Chem. Soc.*, 1994, **116**, 3801–3803.
8 M. Feng and J. Goodenough, *Eur. J. Solid State Inorg. Chem.*, 1994, **31**, 663–672.
9 T. Ishihara, J. A. Kilner, M. Honda and Y. Takita, *J. Am. Chem. Soc.*, 1997, **119**, 2747–2748.
10 M. Li, M. J. Pietrowski, R. A. De Souza, H. Zhang, I. M. Reaney, S. N. Cook, J. A. Kilner and D. C. Sinclair, *Nat. Mater.*, 2014, **13**, 31–35.
11 L. Koch, S. Steiner, K.-C. Meyer, I.-T. Seo, K. Albe and T. Frömling, *J. Mater. Chem. C*, 2017, **5**, 8958–8965.
12 F. Yang, M. Li, L. Li, P. Wu, E. Pradal-Velázque and D. C. Sinclair, *J. Mater. Chem. A*, 2017, **5**, 21658–21662.
13 H. Zhang, A. H. H. Ramadan and R. A. De Souza, *J. Mater. Chem. A*, 2018, **6**, 9116–9123.
14 J. E. ten Elshof, M. H. R. Lankhorst and H. J. M. Bouwmeester, *J. Electrochem. Soc.*, 1997, **144**, 1060–1067.
15 S. J. Benson, R. J. Chater and J. A. Kilner, *Proc. Third Intl. Symp. Ionic and Mixed Conducting Ceramics*, Pennington, NJ, USA, 1997, pp. 596–609.
16 R. A. De Souza and J. A. Kilner, *Solid State Ionics*, 1998, **106**, 175–187.
17 L. Wang, R. Merkle, J. Maier, T. Acartürk and U. Starke, *Appl. Phys. Lett.*, 2009, **94**, 071908.
18 A. Berenov, A. Atkinson, J. Kilner, E. Bucher and W. Sitte, *Solid State Ionics*, 2010, **181**, 819–826.
19 A. Egger, E. Bucher, M. Yang and W. Sitte, *Solid State Ionics*, 2012, **225**, 55–60.
20 A. F. Sammells, R. L. Cook, J. H. White, J. J. Osborne and R. C. MacDuff, *Solid State Ionics*, 1992, **52**, 111–123.
21 K. Nomura and S. Tanase, *Solid State Ionics*, 1997, **98**, 229–236.
22 H. Hayashi, H. Inaba, M. Matsuyama, N. Lan, M. Dokiya and H. Tagawa, *Solid State Ionics*, 1999, **122**, 1–15.
23 M. Mogensen, D. Lybye, N. Bonanos, P. Hendriksen and F. Poulsen, *Solid State Ionics*, 2004, **174**, 279–286.
24 T. Shibasaki, T. Furuya, S. Wang and T. Hashimoto, *Solid State Ionics*, 2004, **174**, 193–203.
25 R. A. De Souza, *Adv. Funct. Mater.*, 2015, **25**, 6326–6342.
26 F. Guyot, P. Richet, P. Courtial and P. Gillet, *Phys. Chem. Miner.*, 1993, **20**, 141–146.
27 P. Gillet, F. Guyot, G. D. Price, B. Tournerie and A. L. Cleach, *Phys. Chem. Miner.*, 1993, **20**, 159–170.
28 B. J. Kennedy, C. J. Howard and B. C. Chakoumakos, *J. Phys.: Condens. Matter*, 1999, **11**, 1479–1488.
29 Y. Gu, K. Rabe, E. Bousquet, V. Gopalan and L.-Q. Chen, *Phys. Rev. B: Condens. Matter Mater. Phys.*, 2012, **85**, 064117.
30 S. A. T. Redfern, *J. Phys.: Condens. Matter*, 1996, **8**, 8267–8275.
31 R. Ali and M. Yashima, *J. Solid State Chem.*, 2005, **178**, 2867–2872.
32 P. M. Woodward, *Acta Crystallogr., Sect. B: Struct. Sci.*, 1997, **53**, 32–43.
33 C. J. Howard and H. T. Stokes, *Acta Crystallogr., Sect. B: Struct. Sci.*, 1998, **54**, 782–789.
34 K. S. Aleksandrov, *Ferroelectrics*, 1976, **14**, 801–805.
35 W. George and R. Grace, *J. Phys. Chem. Solids*, 1969, **30**, 889–892.
36 H. Iwahara, T. Esaka and T. Mangahara, *J. Appl. Electrochem.*, 1988, **18**, 173–177.
37 B. Gautason and K. Muehlenbachs, *Science*, 1993, **260**, 518–521.
38 I. Sakaguchi and H. Haneda, *J. Solid State Chem.*, 1996, **124**, 195–197.
39 T. Bak, J. Nowotny and C. Sorrel, *J. Phys. Chem. Solids*, 2004, **65**, 1229–1241.

40 K. Wright and G. D. Price, *J. Geophys. Res.: Solid Earth*, 1993, **98**, 22245–22253.
41 G. C. Mather, M. Islam and F. Figueiredo, *Adv. Funct. Mater.*, 2007, **17**, 905–912.
42 J. J. Brown, Z. Ke, W. Geng and A. J. Page, *J. Phys. Chem. C*, 2018, **122**, 14590–14597.
43 C. Salles, J. Bassat, J. Fouletier, D. Marinha and M.-C. Steil, *Solid State Ionics*, 2018, **324**, 103–108.
44 S. Marion, A. I. Becerro and T. Norby, *Phase Transitions*, 1999, **69**, 157–168.
45 L. Dunyushkina and V. Gorelov, *Solid State Ionics*, 2013, **253**, 169–174.
46 A. Murashkina, A. Demina, A. Demin, V. Maragou and P. Tsiakaras, *Solid State Ionics*, 2008, **179**, 1615–1619.
47 A. Pedone, G. Malavasi, M. C. Menziani, A. N. Cormack and U. Segre, *J. Phys. Chem. B*, 2006, **110**, 11780–11795.
48 O. Kanert, H. Schulz and J. Albers, *Solid State Commun.*, 1994, **91**, 465–469.
49 M. Kessel, R. A. De Souza and M. Martin, *Phys. Chem. Chem. Phys.*, 2015, **17**, 12587–12597.
50 J. Kaub, J. Kler, S. C. Parker and R. A. De Souza, *Phys. Chem. Chem. Phys.*, 2020, **22**, 5413–5417.
51 F. Cordero, F. Trequattrini, D. Quiroga and P. Silva, *J. Alloys Compd.*, 2021, **874**, 159753.
52 D. B. Schwarz and H. U. Anderson, *J. Electrochem. Soc.*, 1975, **122**, 707–710.
53 A. Hackmann and O. Kanert, *Radiat. Eff. Defects Solids*, 1991, **119–121**, 651–656.
54 F. Cordero, *Phys. Rev. B: Condens. Matter Mater. Phys.*, 2007, **76**, 172106.
55 R. A. De Souza, V. Metlenko, D. Park and T. E. Weirich, *Phys. Rev. B: Condens. Matter Mater. Phys.*, 2012, **85**, 174109.
56 S. P. Waldow and R. A. De Souza, *ACS Appl. Mater. Interfaces*, 2016, **8**, 12246–12256.
57 L. Zhang, B. Liu, H. Zhuang, P. Kent, V. R. Cooper, P. Ganesh and H. Xu, *Comput. Mater. Sci.*, 2016, **118**, 309–315.
58 H. J. Heelweg and R. A. De Souza, *Phys. Rev. Mater.*, 2021, **5**, 013804.
59 K. Gömann, G. Borchardt, M. Schulz, A. Gömann, W. Maus-Friedrichs, B. Lesage, O. Kaïtasov, S. Hoffmann-Eifert and T. Schneller, *Phys. Chem. Chem. Phys.*, 2005, **7**, 2053–2060.
60 R. Meyer, R. Waser, J. Helmbold and G. Borchardt, *Phys. Rev. Lett.*, 2003, **90**, 105901.
61 P. P. Ewald, *Ann. Phys.*, 1921, **369**, 253–287.
62 S. Plimpton, *J. Comput. Phys.*, 1995, **117**, 1–19.
63 J. D. Gale, *J. Chem. Soc., Faraday Trans.*, 1997, **93**, 629–637.
64 S. Amisi, E. Bousquet, K. Katcho and P. Ghosez, *Phys. Rev. B: Condens. Matter Mater. Phys.*, 2012, **85**, 064112.
65 A. I. Becerro, S. A. T. Redfern, M. A. Carpenter, K. S. Knight and F. Seifert, *J. Solid State Chem.*, 2002, **167**, 459–471.
66 M. Schie, R. Waser and R. A. De Souza, *J. Phys. Chem. C*, 2014, **118**, 15185–15192.
67 H. Zhang and R. A. De Souza, *J. Mater. Chem. A*, 2019, **7**, 25274–25278.
68 J. M. Börgers and R. A. De Souza, *Phys. Chem. Chem. Phys.*, 2020, **22**, 14329–14339.
69 N. F. Mott and M. J. Littleton, *Trans. Faraday Soc.*, 1938, **34**, 485.
70 T. Ishigaki, S. Yamauchi, K. Kishio, J. Mizusaki and K. Fueki, *J. Solid State Chem.*, 1988, **73**, 179–187.
71 R. A. De Souza and M. Martin, *Phys. Chem. Chem. Phys.*, 2008, **10**, 2356–2367.
72 H. Schraknepper and R. A. De Souza, *J. Appl. Phys.*, 2016, **119**, 064903.
73 R. A. De Souza, J. Zehnpfenning, M. Martin and J. Maier, *Solid State Ionics*, 2005, **176**, 1465–1471.
74 R. A. De Souza, F. Gunkel, S. Hoffmann-Eifert and R. Dittmann, *Phys. Rev. B: Condens. Matter Mater. Phys.*, 2014, **89**, 241401.
75 K. K. Adepalli, J. Yang, J. Maier, H. L. Tuller and B. Yildiz, *Adv. Funct. Mater.*, 2017, **27**, 1700243.
76 H. Schraknepper, T. E. Weirich and R. A. De Souza, *Phys. Chem. Chem. Phys.*, 2018, **20**, 15455–15463.
77 R.-V. Wang and P. C. McIntyre, *J. Appl. Phys.*, 2005, **97**, 023508.
78 S. Gottschalk, H. Hahn, S. Flege and A. G. Balogh, *J. Appl. Phys.*, 2008, **104**, 114106.
79 H. Bouwmeester, H. Kruidhof and A. Burggraaf, *Solid State Ionics*, 1994, **72**, 185–194.
80 C.-Y. Yoo and H. J. M. Bouwmeester, *Phys. Chem. Chem. Phys.*, 2012, **14**, 11759.
81 V. Metlenko, W. Jung, S. R. Bishop, H. L. Tuller and R. A. De Souza, *Phys. Chem. Chem. Phys.*, 2016, **18**, 29495–29505.
82 J. Claus, M. Leonhardt and J. Maier, *J. Phys. Chem. Solids*, 2000, **61**, 1199–1207.
83 S. Steinsvik, T. Norby and P. Kofstad, *Proc. Electroceramics IV*, Aachen, Germany, 1994, pp. 691–696.
84 V. A. Kolotygin, A. P. Viskup, E. V. Pivak and V. V. Kharton, *Russ. J. Electrochem.*, 2020, **56**, 110–117.
85 J. A. Kilner and R. J. Brook, *Solid State Ionics*, 1982, **6**, 237–252.
86 M. Cherry, M. S. Islam and C. R. A. Catlow, *J. Solid State Chem.*, 1995, **118**, 125–132.
87 V. M. Goldschmidt, *Naturwissenschaften*, 1926, **14**, 477–485.
88 R. D. Shannon, *Acta Crystallogr., Sect. A: Cryst. Phys., Diffr., Theor. Gen. Crystallogr.*, 1976, **32**, 751–767.
89 K. Kreuer, *Solid State Ionics*, 1999, **125**, 285–302.
90 N. Kurita, N. Fukatsu, K. Ito and T. Ohashi, *J. Electrochem. Soc.*, 1995, **142**, 1552–1559.
91 R. A. De Souza, J. A. Kilner and C. Jeynes, *Solid State Ionics*, 1997, **97**, 409–419.
92 J. P. Parras, A. R. Genreith-Schriever, H. Zhang, M. T. Elm, T. Norby and R. A. De Souza, *Phys. Chem. Chem. Phys.*, 2018, **20**, 8008–8015.
93 R. A. De Souza and D. Barboni, *Chem. Commun.*, 2019, **55**, 1108–1111.
94 D. Barboni and R. A. De Souza, *Energy Environ. Sci.*, 2018, **11**, 3266–3274.
95 J. Koettgen, P. C. Schmidt, T. Bučko and M. Martin, *Phys. Rev. B*, 2018, **97**, 024305.